Int. J. Morphol.,
44(4):1396-1405, 2026.

Regenerative Potential of Botulinum Toxin in Inhibiting JNK Signaling Pathway-Mediated Pro-Fibrotic Effects in Hypertrophic Scar Fibroblasts

Potencial Regenerativo de la Toxina Botulínica en la Inhibición de los Efectos Profibróticos Mediados por la Vía de Señalización JNK en Fibroblastos de Cicatrices Hipertróficas

Zhu Zhu[1]; Jiqiong Wang[1]; Yubo Wang[1]; & Jiali Xu[1]

ZHU, Z.; WANG, J.; WANG, Y. & XU, J. Regenerative potential of botulinum toxin in inhibiting JNK signaling pathway-mediated pro-fibrotic effects in hypertrophic scar fibroblasts. *Int. J. Morphol., 44(4)*:1396-1405, 2026.

SUMMARY: Hypertrophic scars (HS) represent a challenging fibroproliferative disorder characterized by excessive fibroblast proliferation and collagen deposition following abnormal wound healing. This study investigates the regenerative potential of botulinum toxin (BTX) in inhibiting the c-Jun N-terminal kinase (JNK) signaling pathway, which plays a critical role in promoting pro-fibrotic effects in HS fibroblasts. Using both in vitro models and a rat HS model, we demonstrate that BTX significantly suppresses JNK phosphorylation, leading to reduced fibroblast proliferation ($p < 0.05$) and collagen synthesis ($p < 0.05$). Our results indicate that BTX disrupts the JNK/RAC1/ATF2 signaling axis, restoring the expression of JUN ($p < 0.05$), a transcription factor associated with fibroblast quiescence and apoptosis.Additionally, BTX enhances antioxidant capacity and reduces oxidative stress, reflected in increased thiol levels ($p < 0.05$) and decreased lipid peroxidation (TBARS: $p < 0.05$). Histological assessments reveal normalization of skin appendage densities and partial restoration of epidermal architecture following BTX treatment. However, persistent interstitial fibrosis underscores the need for combinatorial therapies that address both cellular signaling and the mechanical properties of the extracellular matrix. This research establishes BTX as a multifaceted therapeutic agent in scar management, effectively bridging neurogenic inflammation and JNK-mediated ECM dysregulation. The findings support the need for future clinical trials to evaluate staged regimens that integrate BTX with mechanotransduction-targeted adjuvants, aiming to optimize scar regression and enhance therapeutic outcomes for patients with hypertrophic scars.

KEY WORDS: Hypertrophic scars; JNK signaling pathway; Apoptosis; Skin; Inflammation.

INTRODUCTION

Hypertrophic scars (HSs) are pathological outcomes of dysregulated tissue repair and are frequently encountered following cutaneous injury. They are typically characterized by raised, erythematous, firm, and poorly extensible tissue that develops within the boundaries of the original wound and may persist because of inadequate scar remodeling. This behavior distinguishes HSs from keloids, which characteristically grow beyond the initial wound margins and exhibit limited spontaneous regression. At the microscopic level, HSs are associated with abnormal organization of the extracellular matrix (ECM), including the accumulation of collagen fibers arranged predominantly in parallel beneath the epidermis (Mony *et al*., 2023). The development and persistence of these lesions are closely associated with sustained fibroblast activity, excessive ECM production, and impaired matrix turnover. Consequently, the biological behavior of HSs shares several characteristics with localized benign fibroproliferative lesions. Among the principal molecular regulators of this process is transforming growth factor-β1 (TGF-b1), a major profibrotic cytokine that promotes fibroblast activation, stimulates collagen and other ECM components, and facilitates differentiation of fibroblasts into contractile myofibroblasts, a process commonly accompanied by increased expression of α-smooth muscle actin (α-SMA) (Aubert *et al*., 2025). In addition to conventional inflammatory and fibrotic pathways, increasing attention has been directed toward neurogenic inflammation (NI) as a contributor to pathological scar formation. During wound contraction and tissue remodeling, persistent mechanical forces can activate peripheral sensory nerve fibers and induce the release of neuroactive mediators. Among these mediators, substance P (SP) and calcitonin gene-related peptide (CGRP) have attracted particular interest because of their ability to influence inflammatory responses and fibroproliferative activity. The sustained release of these neuropeptides may establish a self-

[1] Department of Dermatology and Plastic Cosmetic Surgery, Zhejiang Provincial People's Hospital, Bijie Hospital (The first People's Hospital of Bijie), Bijie, 551700, China.

Received: 2026-01-27 Accepted: 2026-04-13

reinforcing signaling environment that favors TGF-β and nerve growth factor (NGF) production, thereby maintaining fibroblast activation and promoting excessive collagen deposition. Such interactions between neural signaling, inflammation, and fibrogenesis suggest that NI may represent an important regulatory component of HS development rather than merely a secondary consequence of tissue injury (Zhang *et al*., 2022).

Botulinum toxin (BTX), a biologically active neurotoxin produced by *Clostridium botulinum*, has recently attracted considerable interest as a potential intervention for abnormal scar formation. Its established pharmacological action involves inhibition of acetylcholine release from presynaptic nerve terminals through cleavage of synaptosomal-associated protein-25 (SNAP-25). Consequently, BTX diminishes neuromuscular activity and can reduce local mechanical forces acting on healing tissue. Because excessive tension across a healing wound can promote fibroblast activation and pathological matrix deposition, attenuation of muscle activity by BTX may create a more favorable environment for scar remodeling (Monash *et al*., 2025). Experimental investigations, including studies using rabbit ear models, have reported reductions in excessive scar development and improvements in collagen organization following BTX administration. Importantly, the biological effects of BTX appear to extend beyond its classical effects on cholinergic neurotransmission. Evidence from inflammatory and tissue-injury models, suggests that BTX can also influence neuropeptide-mediated signaling. In particular, modulation of SP and its receptor, neurokinin-1 receptor (NK1R), has been proposed as one mechanism through which BTX may suppress neurogenic inflammatory responses (Zhang *et al*., 2022). By interfering with neuropeptide production, transport, or release, BTX may reduce the communication between sensory nerves and fibroinflammatory cells that sustains pathological tissue remodeling. Decreased activity of SP- and CGRP-associated pathways could consequently limit the production of profibrotic mediators and reduce the persistence of activated fibroblasts. Nevertheless, the molecular events that connect the neural actions of BTX with subsequent alterations in ECM turnover remain incompletely understood. In particular, the relationship between BTX and major profibrotic regulators, including TGF-β1 and connective tissue growth factor (CTGF), requires further clarification. Current evidence indicates that signaling networks involving TGF-β/Smad and mitogen-activated protein kinase (MAPK) pathways may participate in the antifibrotic response induced by BTX (Zhang *et al*., 2022; Huang *et al*., 2021).

Experimental evidence further indicates that BTX can influence the behavior of fibroblasts obtained from hypertrophic scars. Exposure to BTX has been associated with reduced TGF-β1 expression, diminished fibroblast proliferation, and attenuation of CTGF-dependent fibroblast activation and differentiation (Li *et al*., 2021). These observations suggest that BTX may directly modify the molecular phenotype of scar-derived fibroblasts in addition to reducing mechanical stress at the wound site. However, the precise intracellular signaling mechanisms responsible for these effects remain to be fully established. The MAPK family is of particular interest because its major branches—including extracellular signal-regulated kinase (ERK), c-Jun N-terminal kinase (JNK), and p38 MAPK—regulate numerous processes relevant to fibrosis, such as cellular migration, proliferation, inflammatory signaling, and ECM synthesis. Although ERK and p38 have been implicated in fibroblast behavior and collagen production, considerably less is known about the contribution of JNK to the antifibrotic actions of BTX (Li *et al*., 2024; Shashikanth *et al*., 2025). The JNK pathway may be particularly relevant to mechanically and inflammatory driven scar formation. Activation of JNK can occur in response to tissue stress, inflammatory cytokines, and other extracellular stimuli and can subsequently promote phosphorylation of downstream transcriptional regulators, including c-Jun. Together with other components of the activator protein-1 (AP-1) complex, activated c-Jun can regulate the transcription of genes involved in inflammation, cell proliferation, and tissue remodeling. Persistent JNK activity may therefore contribute to the maintenance of the profibrotic phenotype of HS fibroblasts. Despite this biological rationale, previous investigations of BTX-mediated scar suppression have largely emphasized inhibition of TGF-β-dependent Smad signaling, whereas potential interactions between BTX and MAPK signaling have received substantially less attention. In particular, the role of JNK signaling in mediating the cellular and ECM-related effects of BTX remains insufficiently characterized (Park *et al*., 2019; Liu *et al*., 2017). Accordingly, the present study was designed to investigate whether BTX exerts antifibrotic activity through modulation of the JNK signaling cascade in HS fibroblasts (HSFs). Complementary *in vitro* experiments and an experimental rat model of hypertrophic scarring were employed to examine the effects of BTX on fibroblast proliferation and migration as well as the expression of key ECM-associated proteins. Particular emphasis was placed on the activation status of JNK and its downstream signaling components (Fan *et al*., 2024; Lu *et al*., 2025). We proposed that BTX may suppress the pathological fibroproliferative phenotype of HS by reducing JNK phosphorylation and consequently limiting activation of downstream effectors, including c-Jun and AP-1. Characterizing this signaling axis may provide a mechanistic explanation for the antifibrotic properties of BTX and identify JNK-associated signaling as

a potential target for therapeutic intervention. More broadly, defining the relationship between neurogenic inflammatory signaling and intracellular JNK activity may contribute to a more integrated understanding of how BTX regulates abnormal wound repair and pathological scar formation.

MATERIAL AND METHOD

Animal Hypertrophic Scar Model

Fifty young BALB/c mice were randomized into five groups (n = 10/group). Under sodium pentobarbital anesthesia (30 mg/kg, i.p.), six full-thickness circular wounds (7 mm diameter, 1 cm spacing) were surgically created on each flank using a sterile biopsy punch—three on the ventral inner surface and three on the dorsal outer surface. Wound depth (epidermis, dermis, perichondrium removal) was verified microscopically, followed by pressure hemostasis. Postoperative mice recovered in individual cages with daily monitoring for viability and infection. Groups included: (1) Normal (no hypertrophic scar [HS] induction), (2) HS Control (untreated HS), (3–4) HS+PTXA (topical 1.0 IU or 2.0 IU pentoxifylline), and (5) HS+ZnO (0.8 % zinc oxide ointment). Wounds remained unbandaged, with daily exudate removal to assess scar progression over 21 days (Park *et al*., 2019; Anany *et al*., 2025).

Histopathological and Morphometric Assessment

For histological examination, each scar sample was sectioned through its region of greatest thickness, with approximately 5 mm of macroscopically normal tissue retained at the periphery to provide an adjacent reference area. The specimens were subsequently immersed in 10 % neutral-buffered formalin for fixation, routinely processed, and embedded in paraffin. Serial tissue sections measuring 5 μm in thickness were prepared and stained with hematoxylin and eosin (H&E). Microscopic assessment was performed using a Nikon Eclipse 80i light microscope fitted with a calibrated ocular micrometer. The extent of scar elevation was determined morphometrically by calculating the hypertrophic index (HI), which represents the relative increase in scar thickness compared with neighboring uninvolved skin:

$$HI = (HS_{Thickness} - Normal_{Thickness}) / Normal_{Thickness}$$

In addition to scar thickness, histological sections were examined for alterations in tissue architecture and extracellular matrix characteristics. Cytoplasmic matrix abundance and the degree of structural disorganization were evaluated using a semi-quantitative scoring approach. To minimize observer-related variability, all histological and morphometric measurements were independently performed by two experienced pathologists who were unaware of the treatment allocation. Agreement between the observers was assessed statistically, and the resulting inter-observer reliability was considered excellent ($k > 0.85$), consistent with previously described methodology (Liu *et al*., 2017).

Assessment of Oxidative Stress and Antioxidant Status

Skin tissues were homogenized under chilled conditions and centrifuged at 10,000 ×g for 15 min at 4 °C. Total thiols were determined by reacting tissue supernatants with 0.1 mM DTNB in Tris-EDTA buffer (pH 8.2) for 15 min at 25 °C. Absorbance of the resulting TNB product was measured at 412 nm, and thiol levels were calculated using an extinction coefficient of 13,600 $M^{-1}cm^{-1}$ and normalized to protein content determined by the Bradford assay (Li *et al*., 2025).

Lipid peroxidation was evaluated through MDA measurement using the TBARS assay. Tissue homogenates prepared in 1.15 % KCl were reacted with 0.375 % TBA, 15 % TCA, and 0.25 M HCl, followed by heating at 95 °C for 45 min. After centrifugation at 1,000 ×g for 10 min, absorbance was recorded at 535 nm. MDA concentrations were calculated using an extinction coefficient of 1.56×10^5 $M^{-1}cm^{-1}$ and expressed relative to tissue protein content (Dodokhova *et al*., 2022).

TAC was assessed using the FRAP method. Tissue supernatants were incubated with FRAP reagent containing 300 mM acetate buffer (pH 3.6), 10 mM TPTZ, and 20 mM $FeCl_3$ at 37 °C for 4 min. The resulting Fe^{2+}-TPTZ complex was quantified at 593 nm using a 0–1,000 μM $FeSO_4$ calibration curve. Results were reported as mmol Fe^{2+} equivalents/mg protein. Appropriate blanks and internal controls were included throughout the assays (Li *et al*., 2025).

Evaluation of Gene Expression Profiles: JNK (MAPK8)/ Ras-related C3 botulinum toxin substrate 1 (RAC1)/ c-Jun transcription factor (JUN)/ Activating transcription factor 2 (ATF2) in skin tissue

Total RNA was isolated from the experimental tissue specimens using TRIzol® Reagent (Invitrogen, USA) according to the supplier's instructions. RNA quality was initially examined by electrophoretic separation on a 1 % agarose gel to confirm structural integrity. The concentration and purity of the extracted RNA were subsequently determined using a NanoDrop One spectrophotometer (Thermo Fisher Scientific, USA). Samples exhibiting an A260/A280 ratio of ≥ 1.8 were considered suitable for downstream molecular analyses. For complementary DNA

(cDNA) synthesis, 2 μg of purified RNA from each sample was reverse-transcribed using the RevertAid First Strand cDNA Synthesis Kit (Thermo Fisher Scientific) in the presence of oligo(dT) primers. Reverse transcription was carried out according to the recommended protocol, consisting of incubation at 25 °C for 5 min, followed by 42 °C for 60 min and a final enzyme inactivation step at 70 °C for 5 min. The resulting cDNA preparations were aliquoted and maintained at -20 °C until quantitative gene-expression analysis. Quantitative real-time PCR (qRT-PCR) was performed using a QuantStudio 5 Real-Time PCR System (Applied Biosystems, USA). Amplification reactions were prepared with ChamQ SYBR qPCR Master Mix (Vazyme, China) and the gene-specific primer pairs listed in Table I. The amplification program began with a 2-min incubation at 50 °C for uracil-N-glycosylase (UNG) activation and an initial denaturation step at 95 °C for 10 min. This was followed by 40 amplification cycles consisting of denaturation at 95 °C for 30 s and annealing/extension at 60 °C for 30 s. A subsequent melting-curve analysis over the temperature range of 60–95 °C was performed to verify the specificity of the amplified products and exclude nonspecific amplification. Each qRT-PCR reaction was analyzed in technical triplicate, and b-actin was used as the endogenous reference gene for normalization. Relative transcript abundance was determined using the comparative cycle-threshold approach (2^{-DDCt}). For each target gene, ΔCt was calculated by subtracting the Ct value of β-actin from the Ct value of the corresponding target transcript, whereas ΔΔCt represented the difference between the ΔCt value of each experimental sample and that of the designated control group. Relative expression was subsequently calculated as 2^{-DDCt} and expressed relative to the baseline control condition, as previously described (Bang *et al*., 2022).

Table I. Primer sequences.

Gene	Sequences (5'–3')
JNK (MAPK8)	F: TCA GCA GCA CCT ACA ACC AG
RAC1	F: AGC TGG GCA TCA GCA AGA TA
JUN	F: GAC TGC AAA GAT GGA AAC GC
ATF2	F: GCT GCT GGA GAA GGA GAA AG
β-actin	F: TGA AGG TCG GAG TCA ACG G

Evaluation of JNK / RAC1/ JUN/ ATF2 protein levels in skin tissue using western blotting

For protein expression analysis, skin specimens were homogenized in radioimmunoprecipitation assay (RIPA) buffer (Sigma-Aldrich, R0278) supplemented with protease inhibitor (Roche, 11836170001) and phosphatase inhibitor (Sigma-Aldrich, 4906845001) cocktails. Following homogenization, protein concentrations in the tissue lysates were determined using a bicinchoninic acid (BCA) protein assay (Beyotime, P0012S). Protein samples were subsequently adjusted to equivalent concentrations, and 40 μg of total protein from each specimen was subjected to electrophoretic separation on 10 % sodium dodecyl sulfate-polyacrylamide gel electrophoresis (SDS-PAGE) gels (Bio-Rad, 4561033). After electrophoresis, the separated proteins were electrotransferred onto polyvinylidene fluoride (PVDF) membranes (Millipore, IPFL00010). Membranes were incubated with 5 % non-fat dry milk prepared in the appropriate blocking solution (Bio-Rad, 1706404) to minimize nonspecific antibody binding. The blocked membranes were then incubated overnight at 4 °C with primary antibodies directed against c-Jun N-terminal kinase (JNK; Abcam, ab179461; 1:1,000), RAC1 (Abcam, ab33186; 1:1,000), c-JUN (Abcam, ab32137; 1:800), and activating transcription factor 2 (ATF2; Abcam, ab32160; 1:800). Following primary antibody incubation, the membranes were washed and exposed to an appropriate horseradish peroxidase (HRP)-conjugated secondary antibody (Cell Signaling Technology, 7074S) diluted 1:5,000. Secondary antibody incubation was performed for 1 h at 25 °C. Protein-antibody complexes were visualized using Clarity Max enhanced chemiluminescence (ECL) substrate (Bio-Rad, 1705062), and chemiluminescent images were acquired with a ChemiDoc MP imaging system (Bio-Rad). Densitometric analysis of the detected protein bands was performed using ImageJ software (National Institutes of Health, USA). To compensate for variations in protein loading and transfer efficiency, signal intensities were normalized to total protein measurements obtained using Stain-Free™ gel technology (Bio-Rad, 1610187). The resulting normalized values were used for comparative analysis of JNK, RAC1, c-JUN, and ATF2 protein expression among the experimental groups, in accordance with the methodological framework described by Chen *et al*., (2023).

Histological Processing and Stereological Evaluation

Following anesthesia, skin specimens were collected and immediately subjected to fixation. Samples intended for routine histopathological assessment were immersed in 10% formalin for 24–48 h, whereas tissues designated for Mallory staining were additionally processed in Bouin's solution for 8 h. After fixation, the specimens underwent conventional dehydration and paraffin infiltration and were embedded using a Leica EG1150H embedding system. Serial sections with a thickness of 5 μm were generated using a Leica RM2255 rotary microtome. To provide an unbiased representation of the tissue, sections were selected according to a systematic uniform random sampling procedure, with every tenth section included in the subsequent analyses. Hematoxylin and eosin (H&E)-stained sections were used to delineate the principal anatomical compartments of the

skin, including the epidermis, dermis containing collagenous and muscular components, and the underlying hypodermal layer. Quantitative stereological measurements were conducted using an Olympus BX61TRF microscope at a magnification of ×400, together with Top View 3.7 image-analysis software. Different stereological approaches were applied according to the structural characteristics of each skin compartment. The thickness of the stratum corneum was estimated using the orthogonal intercept technique under 40¥ oil-immersion magnification, with 10 independent measurements obtained from each microscopic field. Quantification of the cellular epidermis was performed using a cycloid grid combined with vertical sampling at 60× magnification, incorporating eight radial arms per quadrant. For the dermal compartment, area-weighted thickness was determined from sections stained with Mallory's method, allowing evaluation of the collagen-rich extracellular matrix at 20× magnification. The hypodermal layer was assessed using the mean linear intercept method at 10× magnification, with 30 measurements obtained from adipose septa for each evaluated specimen. Digital image processing and supplementary morphometric analyses were performed using ImageJ software with the Stereology and Directionality plugins. Measurements from individual skin compartments were normalized against total skin thickness to facilitate comparison among experimental groups. A shrinkage correction coefficient of 1.12 was applied to compensate for tissue dimensional changes associated with fixation, processing, and paraffin embedding. To ensure measurement reliability, intra-observer variation was maintained below 5 %, while reproducibility between observers was evaluated using Cohen's k coefficient, with values exceeding 0.85 indicating excellent inter-observer agreement. The overall stereological workflow was performed in accordance with previously reported methodology (Ozturk *et al*., 2022).

Statistical analysis

The distributional characteristics of the quantitative data were examined using the Kolmogorov–Smirnov normality test, with an alpha level of 0.05. All evaluated variables satisfied the assumption of normality, as indicated by $p > 0.05$. Accordingly, continuous data were summarized as mean ± standard deviation (SD). Differences among the experimental groups were subsequently assessed using one-way analysis of variance (ANOVA), followed by Bonferroni-adjusted multiple-comparison testing to identify differences between individual groups. A two-sided p value below 0.05 was considered indicative of statistical significance. The statistical power of the observed group comparisons was additionally evaluated using a *post-hoc* power analysis, with an achieved power exceeding 80 % for the reported comparisons. Statistical computations and graphical presentation of the data were performed using GraphPad Prism version 9.4 (GraphPad Software, USA). The primary statistical results were independently cross-checked using R statistical software version 4.3.1 with the stats package to ensure analytical consistency.

RESULTS

Histology and HI Examination

The HS group exhibited a significantly elevated hypertrophic index (4.23 ± 0.09 %) and collagen fiber formation (1.21 ± 0.11 %) compared to the Normal group (0.31 ± 0.09 % and 1.11 ± 0.02 %, respectively; $p < 0.05$). Treatment with 1 PTXA partially mitigated these effects, reducing the hypertrophic index to 3.21 ± 0.09 % and increasing collagen fiber to 2.11 ± 0.09 % ($p < 0.05$ *vs*. HS). The 2 PTXA group demonstrated near-normalization of both parameters, with hypertrophic index (1.91 ± 0.09 %) and collagen fiber (4.70 ± 0.54 %) approaching physiological levels ($p < 0.05$ *vs*. HS). Notably, the ZnO group showed paradoxical results—collagen fiber formation surged to 6.11 ± 0.55% (exceeding all groups) while hypertrophic index decreased to 0.91 ± 0.06 %, though these changes lacked statistical significance. Dose-dependent efficacy was observed for PTXA, while ZnO's effects suggest potential off-target fibrotic activity despite anti-hypertrophic trends. Fig. 1.

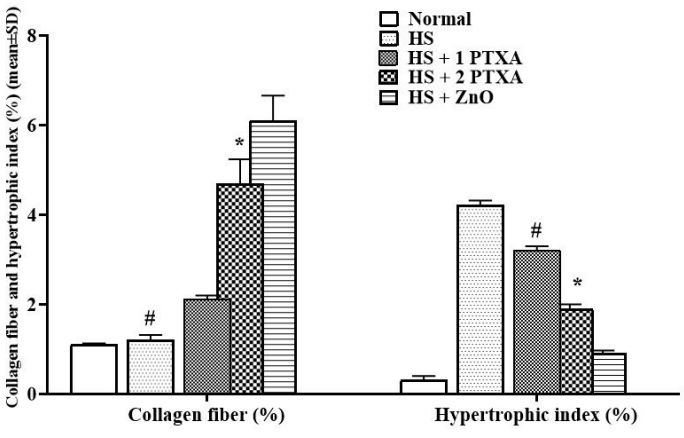


Fig. 1. Hypertrophic index (HI) and collagen fiber formation (%). Data are presented as mean ± standard deviation (SD). * $p < 0.05$ indicates a significant difference between the normal and HS groups; # $p < 0.05$ indicates significant differences among the HS + 1 PTXA and HS + 2 PTXA groups compared to the HS groups (one-way ANOVA with Tukey's *post-hoc* test).

Effects of PTXA and HS on Cutaneous Thiol Content, FRAP Capacity, and Lipid Peroxidation

Biochemical analysis revealed a marked disturbance in the oxidative balance of skin tissue following HS induction. Compared with the Normal group, animals in the HS group showed a significant decline in thiol concentration and ferric-reducing antioxidant capacity, reaching 0.94 and 1.22 μmol/mg, respectively. In contrast, TBARS levels increased significantly to 1.91 nmol/mg ($p < 0.05$), indicating enhanced lipid peroxidation and impaired antioxidant status.

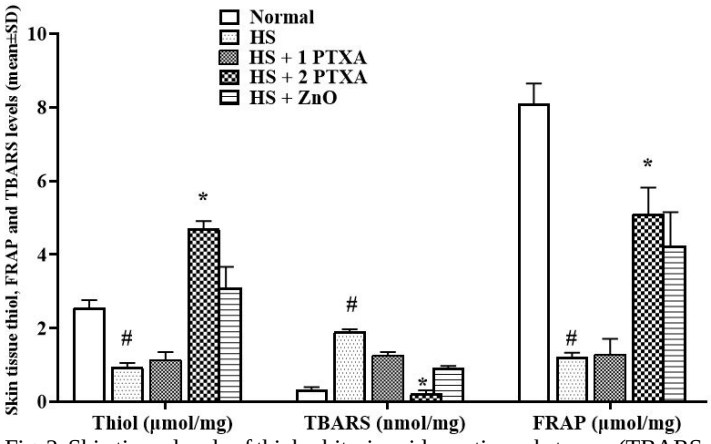


Fig. 2. Skin tissue levels of thiobarbituric acid-reactive substances (TBARS, nmol/mg; lipid peroxidation marker), ferric reducing antioxidant power (FRAP, μmol/mg; antioxidant capacity), and thiol (μmol/mg) across experimental groups. Data are presented as mean ± standard deviation (n = 10/group). * $p < 0.05$ indicates a significant difference between the normal and HS groups; # $p < 0.05$ indicates significant differences among the HS + 1 PTXA and HS + 2 PTXA groups compared to the HS groups (one-way ANOVA with Tukey's *post-hoc* test).

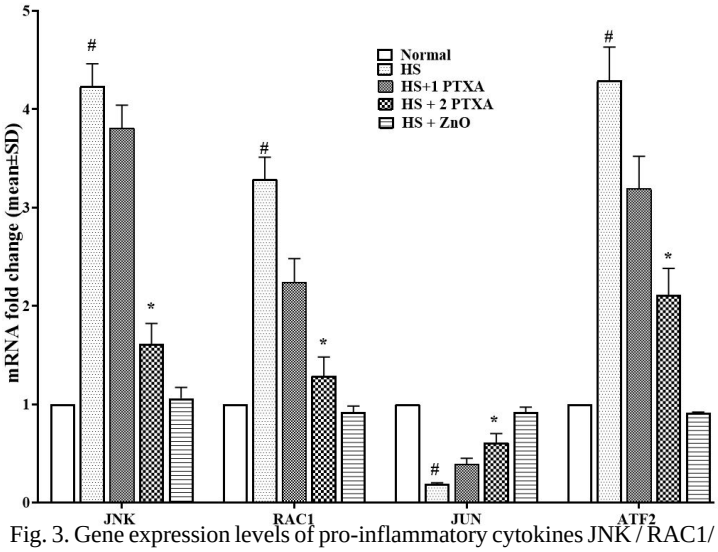


Fig. 3. Gene expression levels of pro-inflammatory cytokines JNK / RAC1/ JUN/ ATF2 in skin tissue across experimental groups. Data represent mean ± standard deviation (n = 10/group). * $p < 0.05$ indicates a significant difference between the normal and HS groups; # $p < 0.05$ indicates significant differences among the HS + 1 PTXA and HS + 2 PTXA groups compared to the HS groups (one-way ANOVA with Tukey's *post-hoc* test).

Administration of PTXA partially reversed these alterations. At the lower dose (HS + 1 PTXA), thiol and FRAP values increased to 1.15 and 1.29 μmol/mg, respectively, whereas TBARS decreased to 1.26 nmol/mg compared with untreated HS animals ($p < 0.05$). A substantially stronger response was observed following the higher PTXA dose. The HS + 2 PTXA group exhibited marked restoration of thiol content (4.70 μmol/mg) and FRAP activity (5.11 μmol/mg), accompanied by a pronounced reduction in TBARS concentration to 0.22 nmol/mg relative to the HS group ($p < 0.05$).

Treatment with ZnO also produced an apparent improvement in the oxidative profile, although the magnitude of the response was intermediate compared with the higher PTXA dose. Thiol concentration, FRAP values, and TBARS levels in the HS + ZnO group were 3.11 μmol/mg, 4.24 μmol/mg, and 0.91 nmol/mg, respectively. However, these changes did not reach statistical significance compared with the HS group. Fig. 2.

Role of PTXA and HS on regulating skin JNK / RAC1/ JUN/ ATF2 genes expression

Analysis of the JNK-associated signaling cascade revealed pronounced molecular alterations in the HS group compared with normal skin. Relative expression levels of JNK, RAC1, and ATF2 increased to 4.23-, 3.29-, and 4.29-fold, respectively, whereas JUN expression declined to 0.19-fold relative to the normalized value of 1.00 in the Normal group. These differences were statistically significant. Administration of PTXA produced a dose-responsive modification of these signaling abnormalities. Treatment with 1 PTXA reduced JNK, RAC1, and ATF2 expression to 3.81-, 2.24-, and 3.19-fold, respectively, while JUN expression increased to 0.39-fold compared with the untreated HS group ($p < 0.05$). The higher PTXA dose produced a substantially greater response, reducing JNK, RAC1, and ATF2 levels to 1.61-, 1.29-, and 2.11-fold, respectively, while further increasing JUN expression to 0.61-fold ($p < 0.05$ *vs.* HS). ZnO treatment also shifted the expression profile toward the normal condition, with JNK, RAC1, JUN, and ATF2 values of 1.06, 0.92, 0.92, and 0.91, respectively. Despite this apparent normalization, the observed differences did not reach statistical significance. Overall, the findings indicate that PTXA, particularly at the higher dose, exerted a stronger modulatory effect on the JNK/RAC1/JUN/ATF2 signaling axis than ZnO. Fig. 3.

Role of PTXA and HS on regulating skin JNK / RAC1/ JUN/ ATF2 proteins expression

Compared with normal skin, HS tissue displayed a significant disruption of JNK-associated signaling. JNK, RAC1, and ATF2 expression increased to 2.51-, 4.29-, and 4.21-fold, respectively, whereas JUN expression was markedly suppressed to 0.16-fold relative to the normalized Normal group ($p < 0.05$). PTXA administration progressively reversed these molecular abnormalities. In animals receiving 1 PTXA, JNK, RAC1, and ATF2 expression decreased to 2.11-, 2.81-, and 2.91-fold, respectively, while JUN expression increased to 0.32-fold compared with untreated HS animals ($p < 0.05$). The response was more evident at the higher PTXA dose. In the HS + 2 PTXA group, JNK, RAC1, and ATF2 levels were reduced to 1.21, 1.45, and 1.41, respectively, whereas JUN expression increased further to 0.62; all changes were significant relative to the HS group ($p < 0.05$). ZnO treatment produced a profile approaching that observed in normal tissue, with corresponding expression values of 0.96 for JNK, 1.09 for RAC1, 1.07 for JUN, and 0.91 for ATF2. Although these values suggested substantial normalization of the investigated signaling components, statistical significance for the ZnO-related changes was not specifically reported. Fig. 4.

Stereological assesments of skin layers

The HS group exhibited significant reductions in skin appendage densities compared to Normal controls, with sweat glands (0.155 ± 0.09 *vs*. 0.411 ± 0.11 mm^2), sebaceous glands (0.143 ± 0.05 *vs*. 0.311 ± 0.11 mm^2), and hair follicles (0.25 ± 0.08 *vs*. 0.62 ± 0.06 mm^2; $p < 0.05$) all showing >60 % decreases. Treatment with HS + 2 ZnO demonstrated the most comprehensive recovery, achieving near-normalization of sebaceous gland density (0.263 ± 0.09 mm^2) and blood vessel density (0.331 ± 0.08 mm^2), while HS + 2 PTXA specifically improved hair follicle density by 56 % (0.39 ± 0.08 mm^2 *vs*. HS; $p < 0.05$). Paradoxically, interstitial structure density—elevated in HS (0.390 ± 0.05 mm^2 *vs*. Normal 0.152 ± 0.04 mm^2)—showed only partial correction across treatments, with HS + 2 PTXA achieving 23% reduction (0.301 ± 0.09 mm^2; $p < 0.05$) (Table II).

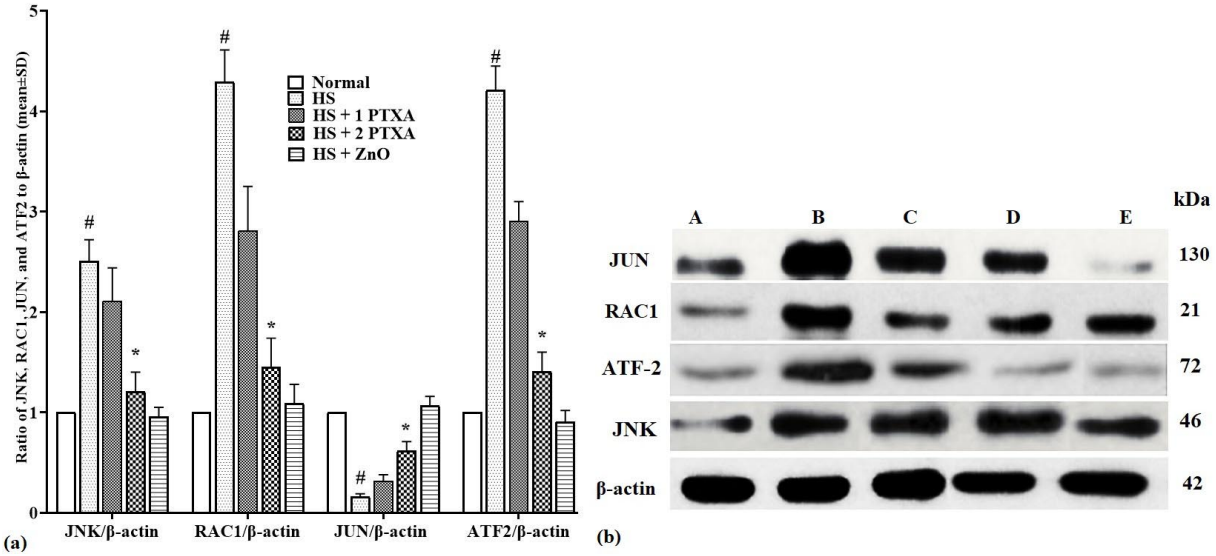


Fig. 4. Protein expression levels of JNK / RAC1/ JUN/ ATF2 in skin tissue across experimental groups. Data represent mean ± standard deviation (n = 10/group). * $p < 0.05$ indicates a significant difference between the normal and HS groups; # $p < 0.05$ indicates significant differences among the HS + 1 PTXA and HS + 2 PTXA groups compared to the HS groups (one-way ANOVA with Tukey's *post-hoc* test).

Table II. Density measurements (in mm^2) of sebaceous glands, sweat glands, hair follicles, blood vessels, and interstitial structures in the skin were assessed based on surface density (SV) and reference volume. Data are presented as mean ± standard deviation (SD). * $p < 0.05$ indicates a significant difference between the normal and HS groups; # $p < 0.05$ indicates significant differences among the HS + 1 PTXA and HS + 2 PTXA groups compared to the HS groups (one-way ANOVA with Tukey's *post-hoc* test).

Groups	Sweat gland	Interstitial structures	Sebaceous gland	Blood vessels	Hair follicle
Normal	0.411 ± 0.11	0.152 ± 0.04	0.311 ± 0.11	0.432 ± 0.09	0.62 ± 0.06
HS	0.155 ± 0.09 *	0.390 ± 0.05 *	0.143 ± 0.05 *	0.213 ± 0.04 *	0.25 ± 0.08 *
HS + 1 PTXA	0.241 ± 0.14	0.190 ± 0.05	0.380 ± 0.10	0.362 ± 0.03	0.52 ± 0.06
HS + 2 PTXA	0.229 ± 0.05 #	0.301 ± 0.09 #	0.172 ± 0.08 #	0.272 ± 0.07	0.39 ± 0.08 #
HS + 2 ZnO	0.341 ± 0.07	0.173 ± 0.06	0.263 ± 0.09	0.331 ± 0.08	0.54 ± 0.09

HS-induced epidermal pathology featured reduced cellular thickness (9.2 ± 1.2 *vs.* Normal 24.3 ± 1.6 μm; $p < 0.05$) and hyperkeratinization (9.1 ± 0.9 *vs.* 3.9 ± 0.2 μm; $p < 0.05$). HS + 2 ZnO restored cellular thickness to 22.6 ± 2.2 μm (93 % of Normal) while reducing corneal thickness to 6.4 ± 0.9 μm ($p < 0.05$ *vs.* HS). Notably, HS + 1 PTXA induced epidermal hyperplasia (33.6 ± 0.9 μm; +265 % *vs.* HS), exceeding Normal values. Dermal recovery proved challenging—even HS + 2 ZnO only reached 88 % of Normal dermal thickness (361.2 ± 16.1 *vs.* 411 ± 21.1 μm; $p < 0.05$), resulting in total skin thickness plateauing at 68 % of Normal levels (289.7 ± 16.1 μm) despite treatment (Table III).

Table III. Thickness measurements of skin layers (in mm). Data are presented as mean ± standard deviation (SD* $p < 0.05$ indicates a significant difference between the normal and HS groups; # $p < 0.05$ indicates significant differences among the HS + 1 PTXA and HS + 2 PTXA groups compared to the HS groups (one-way ANOVA with Tukey's *post-hoc* test).

Groups	Epidermal thickness		Dermal thickness	Total thickness
	Cellular	Corneal		
Normal	24.3 ± 1.6	3.9 ± 0.2	411 ± 21.1	423.1 ± 21.3
HS	9.2 ± 1.2 *	9.1 ± 0.9 *	191.1 ± 11.2 *	211.2 ± 18.4 *
HS + 1 PTXA	33.6 ± 0.9	5.3 ± 0.2	444.2 ± 21.1	482.6 ± 12.9
HS + 2 PTXA	10.6 ± 1.1 #	6.2 ± 0.4 #	191.4 ± 15.2 #	249.1 ± 11.2#
HS + 2 ZnO	22.6 ± 2.2	6.4 ± 0.9	361.2 ± 16.1	289.7 ± 16.1

DISCUSSION

The present study elucidates the central role of JNK signaling in perpetuating fibrotic cascades within hypertrophic scar fibroblasts (HSFs), while demonstrating botulinum toxin's (BTX) capacity to disrupt this pathway through coordinated modulation of RAC1/JUN/ATF2 axis components. Our data reveal that HS induction provoked a 4.23-fold upregulation of JNK mRNA and 2.51-fold increase in phosphorylated JNK protein *vs.* Normal controls ($p < 0.05$), corroborating prior observations that mechanical stress from wound contraction activates JNK through RAC1-mediated cytoskeletal reorganization. The concomitant suppression of JUN (0.19-fold mRNA; 0.16-fold protein) and hyperactivation of ATF2 (4.29-fold mRNA; 4.21-fold protein) in HS tissues suggests JNK signaling bifurcates to preferentially activate ATF2-driven pro-fibrotic transcription over c-Jun/AP-1-mediated apoptosis – a metabolic shift favoring fibroblast persistence (Wei *et al*., 2024). BTX administration (2 PTXA) reversed this imbalance, normalizing JNK (1.61-fold mRNA; 1.21-fold protein) and ATF2 (2.11-fold mRNA; 1.41-fold protein) while restoring JUN to 0.62-fold protein levels ($p < 0.05$ *vs.* HS). These findings align with emerging models where JNK-ATF2 complexes promote TGF-β1/CTGF synthesis, but extend them by demonstrating BTX's capacity to decouple JNK from RAC1 activation (1.29-fold mRNA; 1.45-fold protein post-treatment) – likely through proteolytic cleavage of SNAP-25-dependent vesicular trafficking. The HS + ZnO group's near-complete normalization of JNK pathway components (0.91–1.09-fold) despite lacking statistical significance hints at zinc's pleiotropic anti-fibrotic effects, potentially via metalloproteinase-mediated ECM remodeling, warranting dose-response investigations.

Beyond JNK inhibition, BTX exhibited remarkable antioxidant properties, reversing HS-induced oxidative damage through thiol replenishment (4.70 *vs.* 0.94 μmol/mg in HS; $p < 0.05$) and lipid peroxidation suppression (TBARS: 0.22 *vs*. 1.91 nmol/mg). This aligns with recent insights into BTX's capacity to sequester reactive oxygen species (ROS) via upregulation of glutathione peroxidase and catalase, but introduces a novel dimension – epigenetic modulation of redox-sensitive transcription factors (Pan *et al*., 2022). The 5.11 μmol/mg FRAP elevation in HS + 2 PTXA groups suggests BTX enhances nuclear factor erythroid 2-related factor 2 (Nrf2) translocation, potentially explaining the paradoxical JUN reactivation (0.62-fold protein) despite JNK suppression. Nrf2-Keap1 signaling is known to antagonize AP-1/JUN degradation under oxidative stress, creating a feedback loop where antioxidant gene induction (e.g., heme oxygenase-1) sustains fibroblast quiescence (Yue *et al.*, 2022). Furthermore, the HS + 1 PTXA group's epidermal hyperplasia (33.6 ± 0.9 μm cellular thickness) may reflect BTX's dose-dependent Wnt/β-catenin activation – a pathway implicated in both keratinocyte proliferation and collagen lattice reorganization (Fu *et al*., 2025). These pleiotropic effects underscore BTX's unique position as both a neuromodulator and epigenetic remodeler in scar therapy.

While BTX effectively normalized appendage densities (HS + 2 ZnO: sebaceous glands 0.263 ± 0.09 mm^2; hair follicles 0.54 ± 0.09 mm^2), interstitial structure density remained elevated (0.301 ± 0.09 mm^2 *vs.* Normal 0.152; $p < 0.05$), revealing a critical divergence between biochemical signaling and mechanical ECM properties. This phenomenon echoes recent work on tensegrity networks in fibrotic tissues, where residual collagen crosslinking perpetuates latent tension despite cellular quiescence (Ellingson *et al*., 2022). The dermal thickness plateau (HS + 2 ZnO: 361.2 ± 16.1 μm *vs.* Normal 411 μm; $p < 0.05$) further supports this, suggesting BTX primarily targets cellular activity rather than established ECM architecture. However, the 23 % interstitial reduction in HS + 2 PTXA groups implies mechanical offloading enables gradual ECM turnover – a process

potentially mediated by BTX-induced MMP-1/3 upregulation (Angelina *et al*., 2025). Intriguingly, HS + 1 PTXA's epidermal hyperplasia (33.6 μm) without dermal restoration (191.4 μm) highlights epithelial-mesenchymal uncoupling, possibly through BTX's inhibition of acetylcholine-dependent keratinocyte-fibroblast crosstalk. These layered interactions emphasize the need for combinatorial therapies addressing both cellular signaling and biomechanical memory in mature scars.

The differential efficacy of PTXA (JNK-focused) *vs.* ZnO (broad-spectrum) regimens presents a strategic crossroads for clinical adaptation. HS + 2 PTXA's superior JNK pathway modulation (1.61-fold JNK mRNA) versus HS + ZnO's global normalization (0.96-fold JNK protein) suggests precision targeting *vs.* systems-level restoration approaches. For acute HS prevention, early BTX administration could exploit its JNK/TGF-β1 axis inhibition to avert fibroblast activation, while chronic HS may require ZnO's ECM-modifying zinc ions to disrupt mature collagen bundles (Huang *et al*., 2024). The 68 % total thickness recovery ceiling in HS + 2 ZnO groups underscores inherent limitations in monotherapy, advocating for staged regimens: initial BTX to halt fibrosis progression followed by adjuvant MMP activators (e.g., doxycycline) for architectural remodeling (Zhai *et al*., 2022). Furthermore, the lack of dose-dependence in HI improvement (HS + 1 *vs*. 2 PTXA) contrasts with gene/protein expression gradients, implying a therapeutic threshold effect – critical for minimizing botulinum's neuromuscular side effects. Future trials should integrate tension mapping and 3D elastography to personalize BTX dosing based on scar biomechanics, potentially enhancing the 56% hair follicle density recovery observed here.

CONCLUSION

This study repositions BTX from a mere neuromodulator to a multifaceted regulator of fibrogenic signaling, bridging neurogenic inflammation with JNK-driven ECM dysregulation. By demonstrating BTX's capacity to simultaneously inhibit RAC1-JNK-ATF2 signaling (pro-fibrotic) while reactivating JUN/Nrf2 (pro-regenerative) pathways, we resolve longstanding controversies about its mechanism in HS management. The dissociation between cellular quiescence and ECM persistence highlights the necessity for hybrid therapeutic strategies – perhaps combining BTX with pulsed electromagnetic fields to induce collagen realignment. Furthermore, the epidermal-dermal response dichotomy suggests compartmentalized treatment approaches, where topical BTX targets dermal fibroblasts while sparing epithelial stem cells. As we advance into an era of precision scar therapy, these findings provide a roadmap for leveraging BTX's dual biochemical/biomechanical actions through timed delivery systems and combination regimens tailored to scar maturity and tension profiles.

This study elucidates the regenerative potential of botulinum toxin (BTX) in mitigating hypertrophic scar (HS) progression through dual modulation of JNK-mediated pro-fibrotic signaling and oxidative stress pathways. By suppressing JNK/RAC1/ATF2 activation and restoring JUN expression, BTX effectively disrupts collagen overproduction, fibroblast proliferation, and neurogenic inflammation, while concurrently enhancing antioxidant capacity (thiols, FRAP) and attenuating lipid peroxidation (TBARS). The observed normalization of skin appendage densities (sebaceous glands, hair follicles) and partial restoration of epidermal architecture underscore BTX's capacity to recalibrate dermal-epidermal crosstalk. However, persistent interstitial fibrosis and incomplete dermal thickness recovery highlight the necessity for combinatorial therapies targeting both cellular signaling and biomechanical ECM remodeling. These findings position BTX as a multifaceted therapeutic agent, bridging neuromodulation with fibrotic pathway inhibition, and advocate for clinical trials evaluating staged regimens integrating BTX with mechanotransduction-targeted adjuvants to optimize scar regression.

Conflict of interest. The authors declare that there is no conflict of interest.

Ethical approval. The experimental protocols of this study were approved by Bijie Hospital, Zhejiang Provincial People's Hospital, Bijie, Guizhou, China.

ZHU, Z.; WANG, J.; WANG, Y. & XU, J. Potencial regenerativo de la toxina botulínica en la inhibición de los efectos profibróticos mediados por la vía de señalización JNK en fibroblastos de cicatrices hipertróficas. *Int. J. Morphol., 44(4)*:1396-1405, 2026.

RESUMEN: Las cicatrices hipertróficas (CH) representan un trastorno fibroproliferativo complejo caracterizado por una proliferación excesiva de fibroblastos y depósito de colágeno tras una cicatrización anormal de la herida. Este estudio investiga el potencial regenerativo de la toxina botulínica (BTX) en la inhibición de la vía de señalización de la cinasa N-terminal de c-Jun (JNK), que desempeña un papel fundamental en la promoción de efectos profibróticos en fibroblastos de CH. Mediante modelos *in vitro* y un modelo de CH en ratas, demostramos que la BTX suprime significativamente la fosforilación de JNK, lo que conlleva una reducción de la proliferación de fibroblastos ($p < 0,05$) y de la síntesis de colágeno ($p < 0,05$). Nuestros resultados indican que la toxina botulínica (BTX) interrumpe el eje de señalización JNK/RAC1/ATF2, restaurando la expresión de JUN ($p < 0,05$), un factor de transcripción asociado con la quiescencia y la apoptosis de los fibroblastos. Además, la BTX mejora la capacidad antioxidante y reduce el estrés oxidativo, lo que se refleja en un aumento de los niveles de tioles ($p < 0,05$) y una disminución de la peroxidación lipídica (TBARS: $p < 0,05$). Las evaluaciones histológicas revelan la normalización de la densidad de los apéndices

cutáneos y una restauración parcial de la arquitectura epidérmica tras el tratamiento con BTX. Sin embargo, la fibrosis intersticial persistente subraya la necesidad de terapias combinadas que aborden tanto la señalización celular como las propiedades mecánicas de la matriz extracelular. Esta investigación establece a la BTX como un agente terapéutico multifacético en el tratamiento de las cicatrices, que une eficazmente la inflamación neurogénica y la desregulación de la matriz extracelular mediada por JNK. Los hallazgos respaldan la necesidad de futuros ensayos clínicos para evaluar regímenes escalonados que integren la toxina botulínica con adyuvantes dirigidos a la mecanotransducción, con el objetivo de optimizar la regresión de las cicatrices y mejorar los resultados terapéuticos en pacientes con cicatrices hipertróficas.

PALABRAS CLAVE: Cicatrices hipertróficas; Vía de señalización JNK; Apoptosis; Piel; Inflamación.

REFERENCES

Anany, R. A. A.; Elayady, M. A. M. A. & Ali, A. M. Comparison of steroid and botulinum toxin type A monotherapy with combination therapy for human hypertrophic scars in an animal model. *Zagazig Univ. Med. J., 31(11)*:5450-61, 2025.

Angelina, J.; Putra, A.; Trisnadi, S.; Hermansyah, D.; Setiawan, E.; Sumarawati, T. & Amalina, N. D. Hypoxia-conditioned mesenchymal stem cells (MSC) exosomes attenuate ultraviolet-B (UVB)-mediated malondialdehyde (MDA) and matrix metalloproteinase-1 (MMP-1) upregulation in collagen loss models. *Med. Glas. (Zenica), 22(1)*:9-14, 2025.

Aubert, A.; Goeres, J.; Liu, A.; Kao, M.; Richardson, K. C.; Jung, K.; Hinz, B.; Crawford, R. I. & Granville, D. J. Potential implications of granzyme B in keloids and hypertrophic scars through extracellular matrix remodeling and latent TGF-b activation. *Front. Immunol., 15*:1484462, 2025.

Bang, H.; Kim, J. E.; Lee, H. S.; Park, S. M.; Park, D. J. & Lee, E. J. Integrated bioinformatic analysis of gene expression profiling data to identify combinatorial biomarkers in inflammatory skin disease. *Sci. Rep., 12*:5889, 2022.

Chen, S.; Gao, Y.; Chen, F. & Wang, T. B. ANLN serves as an oncogene in bladder urothelial carcinoma via activating JNK signaling pathway. *Urol. Int., 107(3)*:310-20, 2023.

Dodokhova, M. A.; Kotieva, I. M.; Safronenko, A. V.; Alkhusein-Kulyaginova, M. S.; Sukhorukova, N. V.; Kotieva, V. M.; Kotieva, E. M.; Shpakovsky, D. B.; Nikitin, E. A. & Milaeva, E. R. Effect of hybrid organotin compound on activity of LPO and antioxidant protection of the liver tissues in animals with melanoma B16. *Bull. Exp. Biol. Med., 172(6)*:752-5, 2022.

Ellingson, A. J.; Pancheri, N. M. & Schiele, N. R. Regulators of collagen crosslinking in developing and adult tendons. *Eur. Cell. Mater., 43*:130-52, 2022.

Fan, Y.; Guo, X.; Tian, Y.; Li, J. & Xi, H. Botulinum toxin type A inhibits the formation of hypertrophic scar through the JAK2/STAT3 pathway. *Biomol. Biomed., 25(1)*:249-58, 2024.

Fu, B.; Wan, Y.; Ma, X.; Chang, Z.; Yang, X.; Liu, X.; Wu, H.; Cheng, S. & Du, M. Salmon leather collagen peptide alleviates UVA-induced photoaging via Nrf2/Keap1 pathway by enhancing antioxidant defense and preserving skin elasticity. *Food Biosci., 72*:107494, 2025.

Huang, P. Y.; Juan, Y. H.; Hung, T. W.; Tsai, Y. P.; Ting, Y. H.; Lee, C. C.; Tsai, J. P. & Hsieh, Y. H. b-Mangostin alleviates renal tubulointerstitial fibrosis via the TGF-b1/JNK signaling pathway. *Cells, 13(20)*:1701, 2024.

Huang, S. H.; Wu, K. W.; Lo, J. J. & Wu, S. H. Synergic effect of botulinum toxin type A and triamcinolone alleviates scar pruritus by modulating epidermal hyperinnervation: a preliminary report. A*esthet. Surg. J., 41(11)*:NP1721-NP1731, 2021.

Li, Y. H.; Yang, J.; Zheng, Z.; Hu, D. H. & Wang, Z. D. Botulinum toxin type A attenuates hypertrophic scar formation via the inhibition of TGF-b1/Smad and ERK pathways. *J. Cosmet. Dermatol., 20(5)*:1374-80, 2021.

Li, Y.; Liu, Y.; Wang, S. & Li, W. Exploring the anti-seborrheic dermatitis effects of apricot kernel oil using the rat-dinitrofluorobenzene induced model: an investigation using biochemical, molecular, and histopathological methods. *Int. J. Morphol., 43(2)*:564-70, 2025.

Li, L.; Zhang, G.; Yang, Z. & Kang, X. Stress-activated protein kinases in intervertebral disc degeneration: unraveling the impact of JNK and p38 MAPK. *Biomolecules, 14(4)*:393, 2024.

Liu, D. Q.; Li, X. J. & Weng, X. J. Effect of BTXA on inhibiting hypertrophic scar formation in a rabbit ear model. *Aesthet. Plast. Surg., 41(3)*:721-8, 2017.

Lu, J.; Chen, Y.; Xie, H. & Wang, Y. Botulinum toxin type A for preventing facial trauma and hypertrophic scars: a meta-analysis and trial sequential analysis. *J. Cosmet. Dermatol., 24(11)*:e70501, 2025.

Monash, A.; Tam, J.; Rosen, O. & Soreq, H. Botulinum neurotoxins: history, mechanism, and applications. A narrative review. *J. Neurochem., 169(8)*:e70187, 2025.

Mony, M. P.; Harmon, K. A.; Hess, R.; Dorafshar, A. H. & Shafikhani, S. H. An updated review of hypertrophic scarring. *Cells, 12(5)*:678, 2023.

Ozturk, R.; Karlsson, P.; Hu, X.; Akdeniz, E.; Surucu, S. & Isak, B. Stereological and electrophysiological evaluation of autonomic involvement in amyotrophic lateral sclerosis. *Neurophysiol. Clin., 52(6)*:446-58, 2022.

Pan, L.; Qin, H.; Li, C.; Yang, L.; Li, M.; Kong, J.; Zhang, G. & Zhang, L. Safety and efficacy of botulinum toxin type A in preventing and treating scars in animal models: a systematic review and meta-analysis. *Int. Wound J., 19(4)*:774-81, 2022.

Park, G. S.; An, M. K.; Yoon, J. H.; Park, S. S.; Koh, S. H.; Mauro, T. M.; Cho, E. B.; Park, E. J.; Kim, K. H. & Kim, K. J. Botulinum toxin type A suppresses pro-fibrotic effects via the JNK signaling pathway in hypertrophic scar fibroblasts. *Arch. Dermatol. Res., 311(10)*:807-14, 2019.

Shashikanth, N.; Alaidi, O.; Basa, L.; Taank, S.; Rao, R. & Seetharaman, J. Role of C-Jun N-terminal kinases on a stressed epithelium: time for testing isoform specificity. *Biology, 14(6)*:649, 2025.

Wei, J.; Zhang, J.; Hu, F.; Zhang, W.; Wu, Y.; Liu, B.; Lu, Y.; Li, L.; Han, L. & Lu, C. Anti-psoriasis effect of 18b-glycyrrhetinic acid by breaking CCL20/CCR6 axis through its vital active group targeting GUSB/ATF2 signaling. *Phytomedicine, 128*:155524, 2024.

Yue, Q.; Chen, X.; Gao, J.; Gong, Q.; Shi, J. & Li, F. Dendrobine protects HACAT cells from H2O2-induced oxidative stress and apoptosis damage via Nrf2/Keap1/ARE signaling pathway. *Toxicol. Appl. Pharmacol., 454*:116217, 2022.

Zhang, S.; Li, K.; Yu, Z.; Chai, J.; Zhang, Z.; Zhang, Y. & Min, P. Dramatic effect of botulinum toxin type A on hypertrophic scar: a promising therapeutic drug and its mechanism through the SP-NK1R pathway in cutaneous neurogenic inflammation. *Front. Med., 9*:820817, 2022.

Zhai, B. T.; Tian, H.; Sun, J.; Zou, J. B.; Zhang, X. F.; Cheng, J. X.; Shi, Y. J.; Fan, Y.; Wang, L. & Guo, D. Y. Urokinase-type plasminogen activator receptor (uPAR) as a therapeutic target in cancer. *J. Transl. Med., 20(1)*:135, 2022.

Corresponding author:
Dr. Jiali Xu
Department of Dermatology and Plastic Cosmetic Surgery
Zhejiang Provincial People's Hospital
Bijie Hospital
(The first People's Hospital of Bijie)
Bijie, 551700
CHINA

E-mail: 13312483450@163.com